

# Panel deconvolution of receiver-function gathers: improved images via cross-trace constraints

A. W. Frederiksen

Department of Geological Sciences, University of Manitoba, Winnipeg, Manitoba, Canada. E-mail: frederik@cc.umanitoba.ca

Accepted 2010 November 26. Received 2010 November 25; in original form 2010 August 18

## SUMMARY

A method is presented for deconvolving collections of receiver functions at individual seismic stations. Conventional deconvolution trades-off signal enhancement (through stacking or simultaneous deconvolution) with preservation of directional variation. I replace stacking of traces with minimization of directional derivatives, thus communicating information between traces without stacking and recovering the minimum directional variation required by the data. Directional derivatives are defined by triangulation of the incident horizontal slownesses, computing derivatives at the centre of each triangle. Deconvolution is then posed as a simultaneous inversion for all traces, incorporating directional derivative minimization as cross-trace constraints. The constraints share frequency content between traces, while preserving directional variation. The resulting receiver function gathers have greater intertrace coherence, lower noise levels and higher usable frequencies than standard methods. A decade of teleseismic data at station GAC (Quebec, Canada) are deconvolved using conventional and panel deconvolution; the new technique produces a coherent receiver-function image and reveals complex crust and mantle responses. An extension of the method to recover harmonic coefficients of backazimuthal variation is also included.

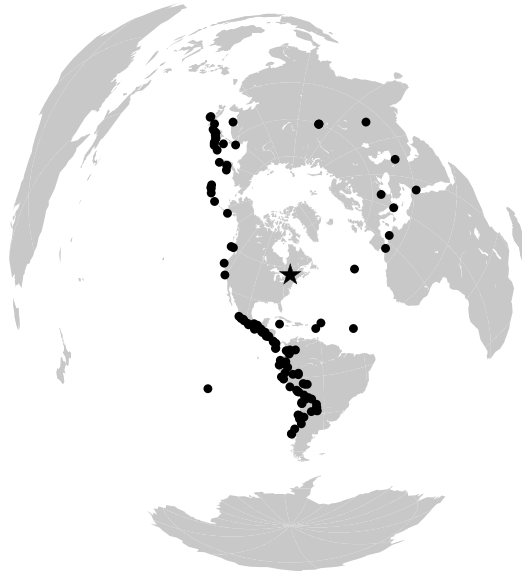
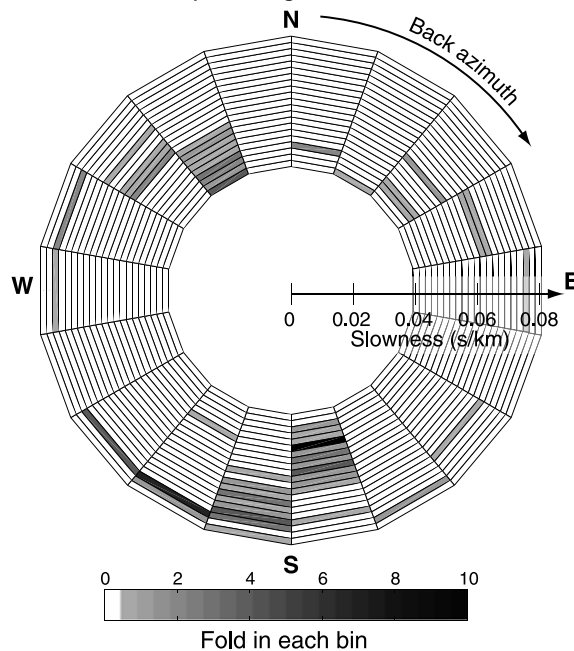
**Key words:** Time-series analysis; Inverse theory; Body waves; Computational seismology.

## 1 INTRODUCTION

The receiver-function technique (Langston 1979) is a widely used passive method for obtaining information on crust and upper-mantle structure beneath seismic recording stations. *P* waves from distant earthquakes interact with receiver-side structure, producing a coda of converted, scattered and reverberated arrivals. However, the relatively long duration of the *P* waveform overlaps with these coda arrivals, making them difficult to distinguish. In the receiver-function approach, an estimate of the incident waveform is deconvolved from the coda, reducing the *P* coda to a series of pulses representing individual arrivals; the result of this deconvolution is called a receiver function. Receiver functions may then be inverted for structure, or used as input to various imaging techniques if sufficient station coverage is available.

A common approach to receiver-function interpretation is to assume a layered subsurface beneath the recording instrument, in which case the receiver function will be dominated by specular *Ps* conversions and reverberations. However, even in the layered case, the receiver function will vary with direction. The arrival times of conversions and reverberations will vary with respect to the angle of the incident ray from vertical (often expressed in terms of the slowness of the incident wave), producing a moveout curve that provides constraints on seismic velocity (see e.g. Zhu & Kanamori 2000). Given a sufficient data set, receiver functions at a given station are often also found to vary with respect to backazimuth as well as slowness. This azimuthal variation is indicative of anisotropy (e.g. Levin & Park 1998), dipping interfaces (e.g. Savage 1998), more complicated 3-D structure or a combination of these factors. Robust recovery of directionally varying receiver functions is important in characterizing subsurface properties. However, under most receiver-function approaches, it is difficult to distinguish between directional variations resulting from structure and variations resulting from deconvolution artefacts, such as variations in the frequency content of the source waveforms.

A typical data set for a single station will include a range of different directions, depending on the station's location with respect to seismogenic regions and with varying event density in different directions. Fig. 1 shows a typical example for a long-running station: station GAC (Ontario, Canada), which is part of the Canadian National Seismograph Network (North & Basham 1993). The upper panel shows the locations of 114 events recorded between 1994 and 2005 and found to be high quality, while the lower shows how these events fall into bins  $20^\circ$  wide in backazimuth and  $0.002 \text{ s km}^{-1}$  wide in slowness. The event distribution is dominated by South and Central America and the western Pacific and overall only a small fraction of the bins are sampled (51 out of 378 possible bins). Of these 51 sampled bins, about

**a) Events recorded at station GAC****b) Binning of GAC events**

**Figure 1.** (a) Locations of high-quality teleseismic earthquakes recorded at station GAC between 1994 and 2005. (b) Binning of these events by backazimuth and slowness. Note that the radial slowness axis in (b) is reversed relative to the epicentral distance in (a), as the most distant events produce near-vertical rays with small slownesses. This data set was previously discussed in Frederiksen *et al.* (2006).

half (24) are sampled by a single trace, while another 12 are sampled twice. The maximum fold achieved in any bin is 10. This data set was previously discussed in Frederiksen *et al.* (2006).

Fig. 2 shows a set of receiver functions obtained from the GAC data set (previously analysed in Frederiksen *et al.* 2006). These receiver functions were obtained by simultaneously deconvolving the traces falling in each sampled bin, in a manner similar to Bostock (1998). Although the traces exhibit considerable lateral coherence, substantial directional variation is visible, particularly on the SH component. Significant noise is also present, as indicated by the appreciable energy visible before zero time. By using broad backazimuthal bins, we have already lost some of the directional information contained in these data. The signal-to-noise ratio of these data could be improved if more directional information were discarded. For instance, the backazimuth could be disregarded completely (eliminating all azimuthal information) and the data could be stacked (or simultaneously deconvolved) purely in slowness bins, giving the best recovery of moveout behaviour. Alternatively, a moveout correction could be applied and the traces stacked in backazimuthal bins (e.g. to determine the orientation

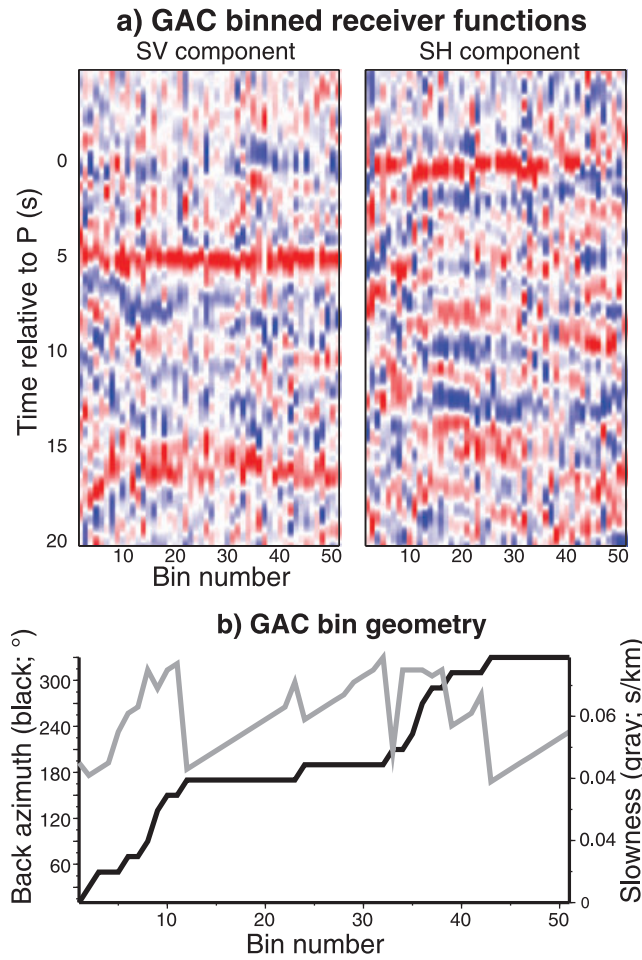


**Figure 2.** (a) Receiver-function data for station GAC, modified from Frederiksen *et al.* (2006). These data were deconvolved using simultaneous deconvolution in backazimuth/slowness bins. (b) Backazimuth and slowness of each bin.

of anisotropic axes). In any event, the trade-off between signal-to-noise ratio and preservation of directional variation is inherent to the problem.

In this paper, I propose what I believe to be a better approach: minimizing the differences between nearby traces through the application of intertrace constraints, and so solving for all receiver functions simultaneously. As I will show below, this approach improves the signal-to-noise ratio while solving for the minimum directional variation required by the data.

## 2 RECEIVER FUNCTION DECONVOLUTION AS AN INVERSE PROBLEM

Let us assume that we have successfully separated a teleseismic wavefield into a  $P$  waveform  $p(t)$  and  $SV$  and  $SH$  waveforms  $s_V(t)$  and  $s_H(t)$ . This may be accomplished by using the vertical, radial and transverse components, by rotating into an orthogonal frame based on the ray direction (Vinnik 1977; Kind *et al.* 1995), or by using the free-surface transfer matrix to recover the wave vector (Bostock 1998) (the method used for the real-data examples in this paper). Regardless of how the component separation is done, each component may be treated as the convolution of a Green's function with a source time function  $i(t)$  representing the incident waveform

$$p(t) = i(t) g_P(t) \quad (1)$$

$$s_V(t) = i(t) g_{SV}(t) \quad (2)$$

$$s_H(t) = i(t) g_{SH}(t) \quad (3)$$

and since  $P$ - $P$  scattered energy is generally weak compared to the primary  $P$  pulse, we will generally assume that  $g_P(t) \approx \delta(t)$ , and so  $p(t) \approx i(t)$ . The receiver function deconvolution problem (where  $s(t)$  and  $g(t)$  are either the  $SV$  or  $SH$  components) then becomes

$$s(t) = p(t) g(t) = \int_{-\infty}^{\infty} p(t - \tau) g(\tau) d\tau \quad (4)$$

for which the unknown is the Green's function  $g_{SV}(t)$ . This is a Fredholm integral equation of the first kind with  $p(t - \tau)$  as the kernel function. For each value of  $t$ , the associated data point  $s_V(t)$  is determined by an inner product with a known kernel  $k(t, \tau) = p(t - \tau)$ , and so the inverse problem is linear. In practice, we work with finite-length sampled sequences, for which convolution remains linear

$$s_j = \sum_{k=1}^{N_g} g_k p_{j-k+1} = \sum_{k=1}^{N_g} A_{jk} g_k, \quad (5)$$

where the kernel matrix is  $A_{jk} = s_{j-k+1}$ . If posed in the frequency domain, the convolution becomes a multiplication and the need for matrix inversion is removed

$$S(\omega) = G(\omega)P(\omega) \quad (6)$$

though note that a convolution of finite-length sequences by spectral multiplication is implicitly circular.

Regardless of the formulation used, then, deconvolution is a linear inverse problem. Although in the ideal case of full-band, noise-free data it is completely determined, in practice it is underdetermined, particularly when the source estimate is noise-contaminated, and so for a given source function and convolved trace, a range of different Green's functions are possible. Much of the variation between deconvolution techniques amounts to different restrictions placed on the Green's function—that is, different forms of regularization of the inverse problem.

In the frequency domain, single-trace deconvolution becomes spectral division of the  $S$  trace by the source estimate. Non-uniqueness arises because both the trace and the source estimate are noisy and the source estimate is bandlimited. A common regularization approach is to set a minimum value (water level)  $w$  for the denominator (Ammon 1991)

$$G(\omega) \approx \frac{S(\omega)P^*(\omega)}{\max(P(\omega)P^*(\omega), w)}. \quad (7)$$

Somewhat more rigorously, applying damping regularization (Bostock 1998) to the inverse problem involves solving the system

$$\begin{pmatrix} S \\ 0 \end{pmatrix} = \begin{pmatrix} P \\ \delta \end{pmatrix} G, \quad (8)$$

where  $\delta$  is the weight assigned to the damping constraint. The least-squares best-fitting solution to this system is similar to the water-level solution

$$G(\omega) \approx \frac{S(\omega)P^*(\omega)}{P(\omega)P^*(\omega) + \delta^2}. \quad (9)$$

Selecting the water level or damping weight to be applied is critical to extracting the maximum of reliable information from the data set. Two time-series are considered to be coherent when they are related by a linear transfer function (the frequency-domain form of an impulse response). In principle, the receiver function is only recoverable at frequencies where we may be confident that the coherence  $\gamma^2$  between the  $P$  and  $S$  traces (Bendat & Piersol 1971)

$$\gamma^2 = \frac{(\langle SP^* \rangle)^2}{\langle PP^* \rangle \langle SS^* \rangle} \quad (10)$$

is not the result of random noise. We may be 95 per cent confident that the coherence is greater than that of random noise when (Thompson 1979)

$$\gamma^2 \geq 1 - 0.05^{2/\lambda}, \quad (11)$$

where  $\lambda = 2m - 2$  is the number of independent degrees of freedom and  $m$  is the number of independent spectral measurements. Note that according to these criteria, the coherence between a single  $P$  and a single  $S$  trace is never significant. Fig. 3(a) shows the coherence between radial and vertical components for a single high-SNR earthquake recording at station GAC, using 3-point spectral averaging to obtain a meaningful coherence measurement. The spectrum of significant coherence (and thus the range of frequencies over which we have information on the Green's function) is far from full-band, with numerous dropouts below the significance level and the highest usable frequency is  $\approx 2.3$  Hz.

Bringing more data into the calculation improves the coherence picture considerably. In Fig. 3(b), 10 radial and vertical traces (the most-populated single bin) from the GAC data set are assumed to reflect a common Green's function. The resulting coherence curve still shows localized dropouts, but overall the coherence appears to be reliable up to about 4 Hz. More surprising is what happens when all traces are included. Given the directional variation in Fig. 2(a), it's clear that the Green's function varies substantially with direction. Nonetheless, when we perform the coherence calculation on all available traces (Fig. 3c), we can see that the coherence is significant across a wide frequency band. Most importantly for deconvolution purposes, all dropouts below 4 Hz are gone. Thus, though individual traces or bins have missing frequencies in their coherence spectra, which will need to be filled in by regularization, the full data set has a fairly complete (though bandlimited) spectrum.

The increased coherence of multiple events may be exploited by stacking receiver functions. A more powerful approach is to assume that all events in a given bin result from the same Green's function, resulting in simultaneous deconvolution (Bostock 1998), which if posed with a damping constraint yields a result similar to before

$$G(\omega) \approx \frac{\sum_{j=1}^N S_j(\omega)P_j^*(\omega)}{\sum_{j=1}^N P_j(\omega)P_j^*(\omega) + \delta^2}. \quad (12)$$

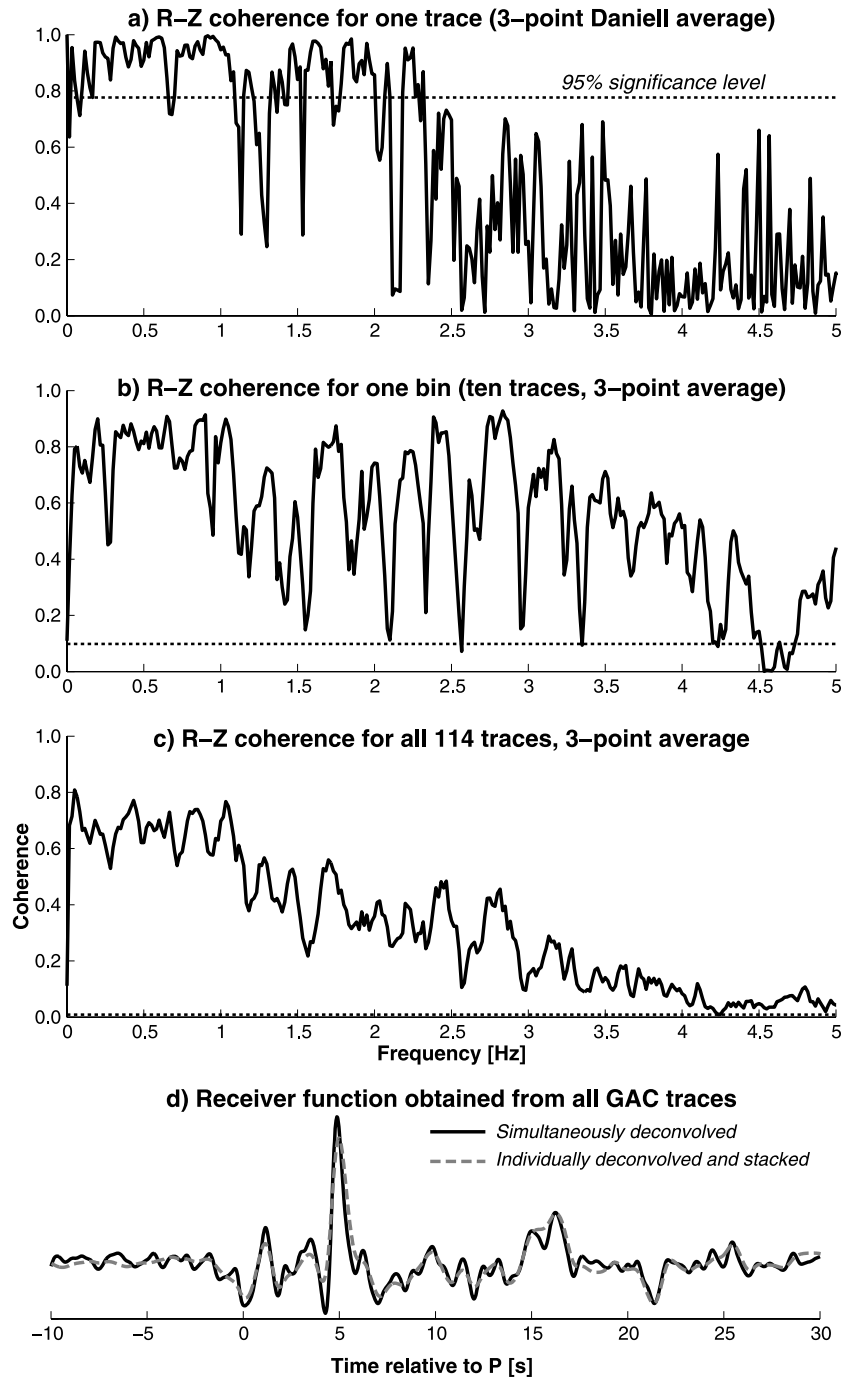


**Figure 3.** Coherence between the radial and vertical components of GAC data spectra, for (a) one trace, (b) one bin and (c) all traces. The dashed line indicates 95 per cent confidence that the two components are coherent. Panel (d) shows the result of deconvolving all  $P$  from all  $SV$  components, either simultaneously (solid) or trace-by-trace, followed by stacking (dashed).

Fig. 3(d) shows the result of simultaneously deconvolving all GAC traces, along with the result of stacking individual-trace deconvolutions (which gives a very similar result). Stacking or simultaneous deconvolution are all-or-nothing approaches; traces in a given bin are assumed to have identical Green's functions, while no similarity to adjacent bins is assumed. A trade-off between directional resolution (for which small bins are best) and quality of individual receiver functions (best with large fold) is inherent in this approach. Simultaneous deconvolution may be thought of as an end-member to a range of problems: when deconvolving simultaneously, each trace can be considered to have its own Green's function  $G_i$ , provided that all of these are constrained to be equal (e.g. by incorporating additional equations  $G_i = G_j$  with high weights). The opposite end-member is individual-trace deconvolution, in which no similarity in between the Green's functions is enforced. Cross-trace constraints, as described in the next section, introduce the possibility of a middle ground.

### 3 CROSS-TRACE CONSTRAINTS

The trade-off between directional resolution and receiver-function quality may be better managed by requiring receiver functions from different events to be similar in proportion to the similarity of their directions. If we have a set of  $N$  events each coming from a backazimuth  $\phi_j$  with a slowness  $q_j$ , then our forward problem is

$$s_j(t) = p_j(t) g(t; \phi_j, q_j) \quad (13)$$

the Green's function being taken to be a function of direction. Posed this way, we can impose constraints on the directional variation of the Green's function. The backazimuth and slowness may be replaced by the north–south and east–west components of the slowness vector  $q_N^{(j)}$  and  $q_E^{(j)}$ , allowing us to pose the constraint equations

$$\frac{\partial G}{\partial q_N} = 0 \quad (14)$$

$$\frac{\partial G}{\partial q_E} = 0 \quad (15)$$

that is, minimizing the derivative of the Green's function (here written in the frequency domain) with respect to each slowness component.

Each trace represents a point in  $(q_N, q_E)$  space. Since we only have data at these discrete points, we'll only seek to recover the Green's function at the sampled points. To recast the derivatives in terms of individual sample points  $G_j$  rather than a continuous function, we need to minimize discrete estimates of the derivatives. Finite-difference approximations of derivatives are generally given in terms of equally spaced samples. In this case, the sampling is imposed by the data and is likely to be highly irregular (Fig. 4). We can, however, tessellate the  $(q_N, q_E)$  plane with a series of non-intersecting triangles whose corners lie at each of the sampled slowness points. If the triangles are chosen to be as close to equilateral as possible, this tessellation is known as a Delaunay triangulation (Okabe *et al.* 1992).

The Delaunay triangulation of the  $(q_N, q_E)$  plane provides us with a natural way to pose the derivative of the Green's function. For each triangle with corners A, B and C, we have a set of three slowness points  $(A_N, A_E)$ ,  $(B_N, B_E)$  and  $(C_N, C_E)$  at which we want to recover the Green's functions  $G_A$ ,  $G_B$  and  $G_C$ . If we treat the Green's function as being planar over the triangle, then the slope of the plane in the N–S and E–W directions is defined to be

$$\frac{\partial G}{\partial q_N} \approx \frac{C_E - B_E}{n_z} G_A + \frac{A_E - C_E}{n_z} G_B + \frac{B_E - A_E}{n_z} G_C \quad (16)$$

$$\frac{\partial G}{\partial q_E} \approx \frac{B_N - C_N}{n_z} G_A + \frac{C_N - A_N}{n_z} G_B + \frac{A_N - B_N}{n_z} G_C, \quad (17)$$

where the denominator  $n_z$ , representing the vertical coordinate of a unit normal to the plane formed by the triangle, is given by

$$n_z = A_E(C_N - B_N) + B_E(A_N - C_N) + C_E(B_N - A_N) \quad (18)$$

Setting  $\partial G / \partial q_N = 0$  and  $\partial G / \partial q_E = 0$ , eqs (16) and (17) become constraints relating three traces (A, B and C). The denominator  $n_z$  is crucial, in that it ensures that the equations are weighted correctly. Since we're minimizing an estimate of the derivative rather than a simple

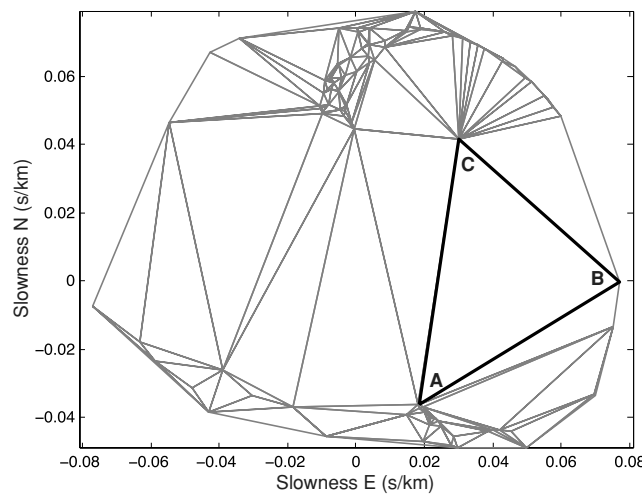


**Figure 4.** Delaunay triangulation of the slowness plane for the GAC data set. Each vertex represents the N–S and E–W slowness of a single event. As the slowness vector is oriented in the direction of wave propagation, events are plotted  $180^\circ$  away from their backazimuthal placement in Fig. 1b. The vertices A, B and C of a sample triangle are highlighted. The derivatives of  $G$  with respect to  $q_N$  and  $q_E$  are posed at the centre of the triangle, in terms of the values at the corners.

difference, changes in  $G$  across a large triangle (i.e. a large change in incident ray angle) will be penalized less severely than changes in  $G$  between nearby traces. For each triangle in the triangulation, we obtain two constraint equations, one in the N–S direction and the other in the E–W directions. Assembling all of these constraints into a matrix, we introduce the intertrace constraint matrix  $\mathbf{N}$ , for which the constraints are posed as  $\sum_j N_{ij} G_j = 0$ .  $\mathbf{N}$  will have two rows for each triangle in the Delaunay triangulation.

Since we now have a system of constraints relating the Green's functions for different traces, deconvolution becomes a joint inversion for all traces simultaneously. Two more matrices are required to pose the complete inverse problem. In the frequency domain, the data are incorporated by recognizing that the individual spectral products  $S_i = G_i P_i$  may be rewritten as a matrix product  $S_i = \sum_j M_{ij} G_j$ , where  $M_{ij} = \delta_{ij} P_i$ .  $\mathbf{M}$  is thus a frequency-dependent diagonal matrix, while the cross-trace constraint matrix  $\mathbf{N}$  is frequency-independent but non-diagonal. Even with cross-trace constraints applied, some damping will be required to fully stabilize the problem, to account for frequencies which are not sampled by any trace. The damping is incorporated in the form of an identity matrix:  $\mathbf{I}G = 0$ . The fully posed problem to be solved in a least-squares sense is then

$$\begin{bmatrix} \mathbf{M} \\ \mu \mathbf{N} \\ \delta \mathbf{I} \end{bmatrix} \mathbf{G} = \begin{bmatrix} \mathbf{S} \\ \mathbf{0} \\ \mathbf{0} \end{bmatrix}, \quad (19)$$

where  $\mathbf{G}$  is a vector of all Green's functions at a single frequency,  $\mathbf{S}$  is a vector of all  $S$  responses at the same frequency and  $\mu$  and  $\delta$  are weights applied to the cross-trace and damping constraints, respectively. Eq. (19) must be solved once for every frequency of interest. The resulting set of Green's functions will contain only those directional variations required by the data, assuming the regularization weights are correct. The use of the cross-trace constraints proposed here may be thought of as biasing the deconvolution to find the minimum directional variation necessary to accommodate the data.

#### 4 PANEL DECONVOLUTION: IMPLEMENTATION AND SYNTHETIC TESTS

I implemented the inverse problem, as summarized in eq. (19), in MATLAB. The cross-trace constraints are calculated using MATLAB's built-in Delaunay triangulation and the inversion is performed in a least-squares sense in the frequency domain. From here on, I will refer to the simultaneous deconvolution of multiple traces using cross-trace constraints as 'panel deconvolution', as the technique solves for an entire panel of receiver functions in one operation.

The basic assumption of the panel deconvolution approach is that the Green's function varies slowly with angle—that is, that we do not expect sudden changes in the Green's function over small variations in direction. To verify this, I generated a synthetic set of Green's functions using the sharpest possible subsurface structure: a point scatterer. Fig. 5(a) shows synthetic Green's functions [obtained using a ray-Born approach; see Frederiksen and Revenaugh (2004)] for a model containing two point scatterers: a  $P$  velocity perturbation located 11 km north of the station at 14 km depth and an  $S$  velocity perturbation located 2 km west of the station at 10 km depth. No interfaces were included in the model, and so the Green's function contains only the primary  $P$  wave, forward-scattered waves from the interaction of the primary wave with point scatterers and backscattered waves from the interaction of free-surface  $P$  and  $S$  reflections with the scatterers. The trace geometry (backazimuths and slownesses) was taken to correspond to the bins used for the GAC data in Fig. 2.

To test the effect of panel deconvolution, each synthetic Green's function was convolved with a different  $P$  component from the GAC data set (to represent a realistic primary pulse) and Gaussian random noise (with a standard deviation of 10 per cent of peak trace amplitude) was added to all components. The resulting synthetic data set was then subjected to both conventional damped deconvolution (Fig. 5b) and panel deconvolution (Fig. 5c) using the  $P$  component of the noisy synthetic as the primary. The receiver functions obtained using either deconvolution method will be expected to differ from the input Green's function due to the band-limited nature of the source function, the incoherent random noise added to both the vertical and radial components and the coherent noise introduced by deconvolving the vertical component (which contains a component of scattered waves) rather than the true primary pulse.

The first observation to make from Fig. 5 is that even for a crustal point scatterer (close to a worst-case scenario for receiver-function analysis), the Green's functions show considerable lateral coherence, particularly for the later backscattered phases. The coherent arrivals at  $\approx 1.2$ , 4.5 and 6 s represent  $P$ – $S$  scattering from the  $S$  velocity perturbation; the much less coherent energy visible on the transverse component in the 0.5–1.5 and 5–6 s ranges represents  $P$ – $P$  scattering from the  $P$  perturbation. Receiver function analysis typically assumes that the  $P$  coda is dominated by  $P$ – $S$  converted energy, which (in this example at least), tends to produce laterally coherent arrivals even from point-scatterer sources. Comparing panels B and C, the panel deconvolution approach clearly does a superior job of suppressing incoherent noise, and does an excellent job (within the band limitation imposed by the source wavelet) of recovering the major laterally coherent arrivals with correct timing and polarity, and with consistent pulse width and amplitude. In particular, the 1.2 and 6 s arrivals are hard to see in the radial component of panel B, but quite coherent in panel C. Note, however, that some narrow regions of low amplitude, laterally coherent noise are visible in the panel deconvolution result, presumably representing artefacts introduced by the cross-trace constraints. It may not be safe to interpret narrow windows of coherency in panel deconvolution results, if they are low in amplitude.

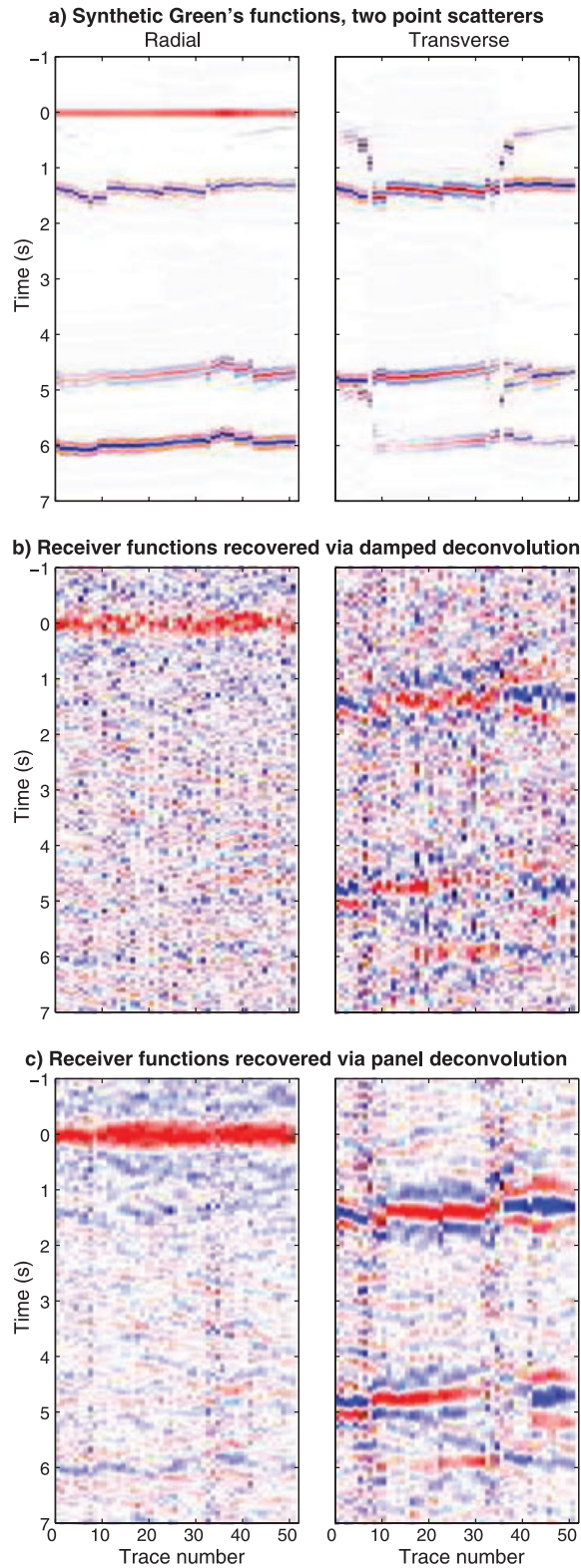


**Figure 5.** Synthetic test of panel deconvolution for a model containing two point scatterers. The backazimuths and slownesses are taken from the binned GAC traces in Fig. 2. (a) Synthetic impulse response generated using a ray-Born approach (Frederiksen and Revenaugh 2004). (b) Impulse response from (a), convolved with P components from the GAC data set and then deconvolved using a conventional approach (no cross-trace constraints). (c) Same as (b), except that the deconvolution was performed using panel deconvolution.



Some of the strongest directional changes observed in receiver functions result from anisotropic layers. The SH-component amplitude of a  $P_s$  conversion from an anisotropic layer with no velocity contrast will display a  $\sin 2\phi$  behaviour with respect to backazimuth, with two positive and two negative lobes and four zero crossings. To verify whether the intertrace regularization obscures these zero crossings, I generated synthetic data [using a ray-theoretical method described in Frederiksen & Bostock (2000)] for a three-layer model consisting of an isotropic crust 35 km thick, an anisotropic upper-mantle layer 40 km thick with a N–S horizontal fast axis and an isotropic mantle half-space with velocity equal to that of the anisotropic layer. As in the previous synthetic example, the synthetic was generated assuming a trace geometry corresponding to the GAC event bins and then was convolved with primary waveforms taken from the GAC data set.

Fig. 6 shows the synthetic Green's function before convolution (panel a) and the result of deconvolution using conventional (b) and cross-trace regularized (c) methods. It is clear from panel (c) that the sign changes have been preserved. In this example, the improvement in quality from panel deconvolution is less dramatic than in the scattering example, though recovery of the faint arrival at  $\approx 8$  s on the SV component is improved. Arrivals are also somewhat less diffuse in the panel-deconvolved case. It is plain from both synthetic tests that panel deconvolution will not obscure the types of backazimuthal variations that we would expect from realistic Earth structures.

## 5 PANEL DECONVOLUTION: REAL DATA

As a real-world test of the panel deconvolution approach, I applied the panel deconvolution technique to the GAC data set discussed above. The data were deconvolved with separately weighted intertrace and damping constraints, recovering 114 individual receiver functions. For plotting purposes, the 114 receiver functions were subsequently stacked into the same set of 52 bins used in the conventional deconvolution (Fig. 2b).

Fig. 7 shows the result of three panel deconvolutions of the GAC data with different parameter settings. In Fig. 7(a), the intertrace constraint weight was set to zero, thus deconvolving without intertrace regularization. The frequency band used was 0.05–0.5 Hz, the same as in the binned deconvolution. The results are somewhat worse than for the binned deconvolution (compare with Fig. 2, due to the use of a common damping weight across all traces and the lack of simultaneous deconvolution).

Inclusion of cross-trace constraints improves the picture significantly. Appropriate levels for the regularization constraints were determined by examining the trade-off between the intertrace 'steepness' of the image (the root-mean-square sum of the intertrace derivatives) and the misfit to the original  $SV$  and  $SH$  components. With well-chosen values of  $\mu$  and  $\delta$  (in this case, 0.025 and 0.06, respectively), a remarkable improvement in the signal-to-noise ratio was achieved (Fig. 7b). With random fluctuations between traces greatly reduced, much more detail is visible on both  $SV$  and  $SH$  panels. Arrivals are not identical across all traces, and moveout is present, indicating that the arrivals are not artefacts introduced by the cross-trace constraints. The amplitude of noise artefacts may be seen by examining the receiver functions at negative times, from which it is apparent that the major features of the receiver-function panel are robust.

With the cross-trace constraints in place, I tested the effect of extending the frequency range. Fig. 7(c) shows the result of extending the upper cut-off frequency to 1 Hz. With conventional deconvolution, a 1 Hz cut-off gives an unacceptable noise level. Panel deconvolution, however, still gives good results in this range, revealing a more complicated system of arrivals. At 2 Hz, obvious artefacts became visible (indicated by apparent coherent arrivals at negative times) and so frequencies beyond 1 Hz were not included in the figure.

It is worth noting that some of the benefits of panel deconvolution may be achieved (in less controlled fashion) by spatial smoothing of receiver functions obtained using more established techniques. Fig. 8 shows the result of smoothing the binned receiver functions from Fig. 2. Each smoothed output trace is a weighted sum of the unsmoothed traces, the weights being obtained from a Gaussian of length  $0.02 \text{ s km}^{-1}$  in the slowness plane, centred on the slowness point corresponding to the output trace. The result is, in this case, not greatly inferior in appearance to Fig. 7(b). The panel-deconvolved result is, however, known to fit the data, being the result of a data inversion, while in the smoothed case, the data fit may be degraded. The choice of smoother length is difficult to justify in any formal way; in this particular case, I had the benefit of the panel-deconvolved result to use as a guide.

The improved signal-to-noise ratio and frequency content obtained using panel deconvolution changes the structural picture at GAC. Figs 2 and 7(b) show, for the most part, the same basic arrivals, which remain a good match to the synthetic shown in Frederiksen *et al.* (2006) (though in the latter case the improved SNR lends more confidence to some of the weaker arrivals). Higher frequencies in Fig. 7(c), however, reveal more arrivals. There are now several coherent arrivals visible prior to the Moho  $P_s$  conversion (i.e. before  $\approx 5$  s) on the  $SH$  panel; this is indicative of dipping, non-planar or anisotropic structure within the crust. The Moho multiple at  $\approx 15$  s on the  $SV$  component is now found to be a double arrival on some traces, which may reflect multipathing due to Moho topography. Some additional arrivals (such as energy from 5 to 7 s on traces 10–20 of the  $SH$  panel) are only visible on some traces and may reflect 3-D structures. Simple 1-D or dipping-layer modelling will be insufficient to treat these arrivals; the significance of the higher-frequency features may be clarified by the use of 3-D imaging techniques.

## 6 ALTERNATIVE FORMULATIONS: HARMONIC DECOMPOSITION

Posing receiver function deconvolution as the recovery of a spatial function  $G(\omega; \phi, q)$  has broader uses than intertrace regularization. By parametrizing the spatial variation of  $G$ , we can potentially recover receiver functions at geometries not corresponding to those of the available

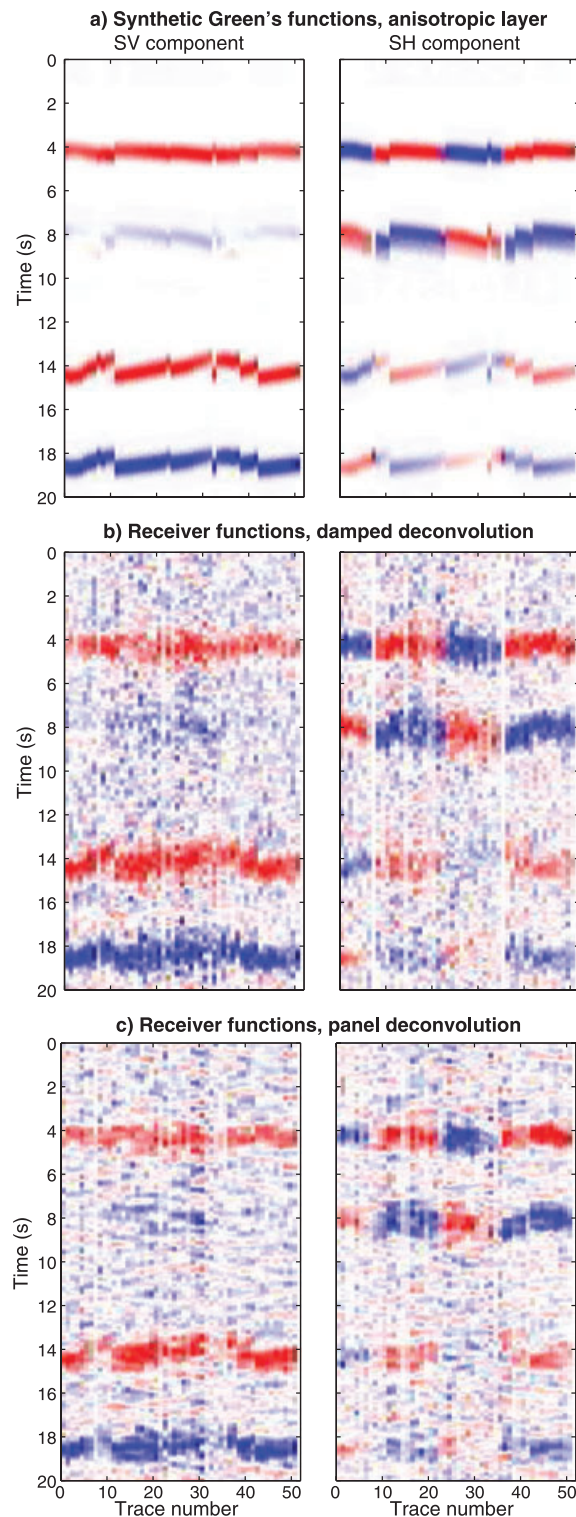


**Figure 6.** Synthetic test of panel deconvolution for a model containing an anisotropic upper-mantle layer with a horizontal fast axis. (a) Synthetic impulse response. (b) Conventional receiver functions corresponding to (a), obtained in a manner similar to Fig. 5(b). (c) Same as (b), except that panel deconvolution was used.

earthquakes. We could potentially use this approach to interpolate receiver functions onto a regularly spaced grid of backazimuth and slowness, though regions not sampled by earthquakes would be poorly constrained.

A more promising approach is to simplify the spatial parametrization of  $G$ , to recover those spatial variations that are most interpretable in terms of structure. If we assume a layered medium that may contain anisotropy and dipping interfaces, the resulting pattern of receiver

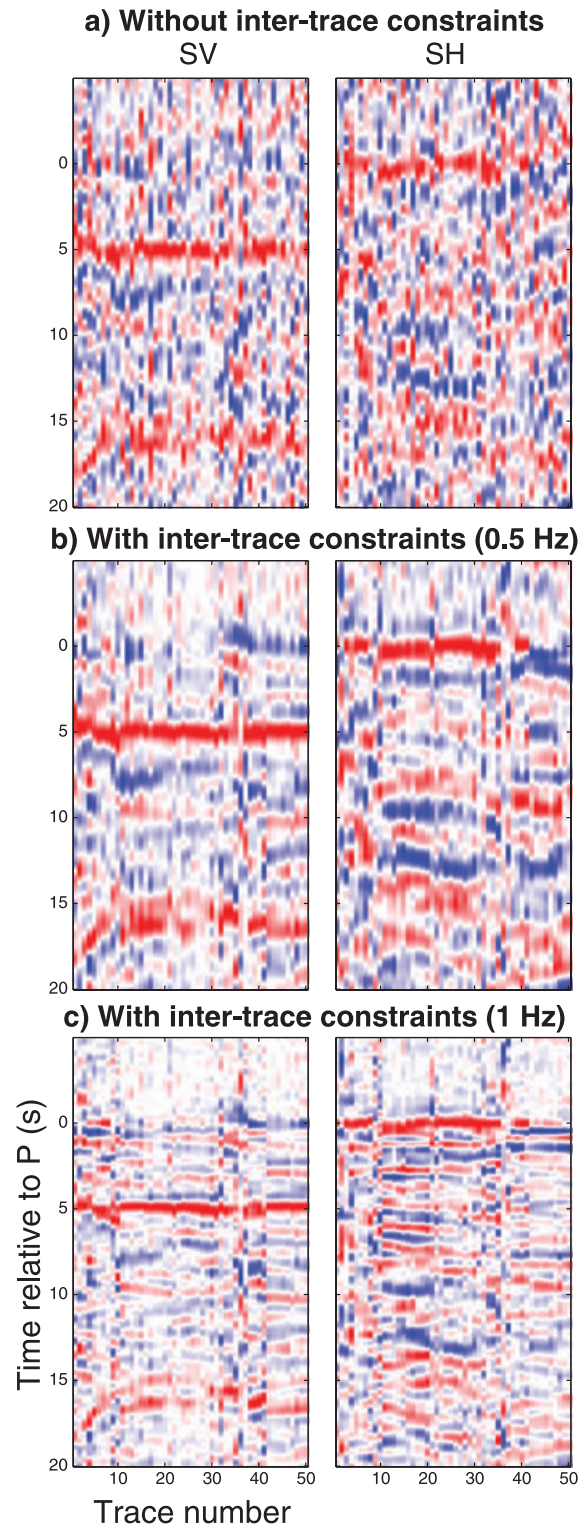


**Figure 7.** GAC receiver functions, obtained using panel deconvolution. (a) Zero weight for intertrace constraints; noisier than Fig. 2 due to the lack of simultaneous deconvolution and the use of a single common damping weight. (b) As (a), with intertrace constraints. The frequency band (0.05–0.5 Hz) is the same as for Fig. 2. (c) As (a), with intertrace constraints and a higher cut-off frequency (1 Hz). Conventional deconvolution gave poor results with this cut-off. Bins are as in Fig. 2.

functions displays two-lobed (interface dip or plunging anisotropic axis) or four-lobed (horizontal anisotropic axis) symmetry with respect to backazimuth (see e.g. Levin & Park 1998; Savage 1998; Frederiksen & Bostock 2000). These patterns may be recovered by harmonic analysis of the backazimuthal variation (e.g. Girardin & Farra 1998; Agostinetti *et al.* 2008). Usually, this harmonic analysis is done through post-deconvolution stacking; however, it may be done at the deconvolution level by

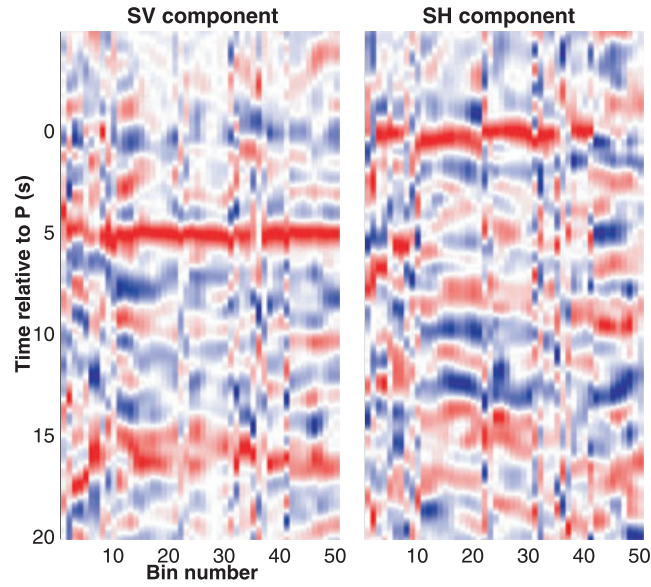


**Figure 8.** GAC bin-deconvolved data from Fig. 2, smoothed spatially using a Gaussian. Compare with Fig 7(b).

posing

$$G(\omega; \phi, q) = G_1(\omega) + G_2(\omega) \cos \phi + G_3(\omega) \sin \phi + G_4(\omega) \cos 2\phi + G_5(\omega) \sin 2\phi, \quad (20)$$

where  $G_1$  represents the directionally invariant component of the receiver functions,  $G_2, G_3$  represent two-lobed backazimuthal patterns and  $G_4, G_5$  represent four-lobed patterns. The forward problem for  $N$  traces  $P_j, S_j$  with backazimuth  $\phi_1, \phi_2, \dots, \phi_N$  then becomes

$$\begin{pmatrix} S_1 \\ S_2 \\ \vdots \\ S_N \end{pmatrix} = \begin{pmatrix} P_1 & P_1 \cos \phi_1 & P_1 \sin \phi_1 & P_1 \cos 2\phi_1 & P_1 \sin 2\phi_1 \\ P_2 & P_2 \cos \phi_2 & P_2 \sin \phi_2 & P_2 \cos 2\phi_2 & P_2 \sin 2\phi_2 \\ \vdots & \vdots & \vdots & \vdots & \vdots \\ P_N & P_N \cos \phi_N & P_N \sin \phi_N & P_N \cos 2\phi_N & P_N \sin 2\phi_N \end{pmatrix} \begin{pmatrix} G_1 \\ G_2 \\ \vdots \\ G_5 \end{pmatrix}. \quad (21)$$

This formulation does not require explicit cross-trace regularization because the harmonic formulation implicitly requires the harmonic parameters to depend on the entire set of traces. We will only require damping regularization, achieved by augmenting eq. (21) with a weighted  $5 \times 5$  identity matrix.

Fig. 9 shows the result of performing an inversion for harmonic components using the GAC data set; the magnitudes of the directionally varying components (i.e.  $\sqrt{G_2^2 + G_3^2}$  and  $\sqrt{G_4^2 + G_5^2}$ ) are shown in Fig. 10. The  $\phi$ -periodic magnitude (lower traces) contains significant

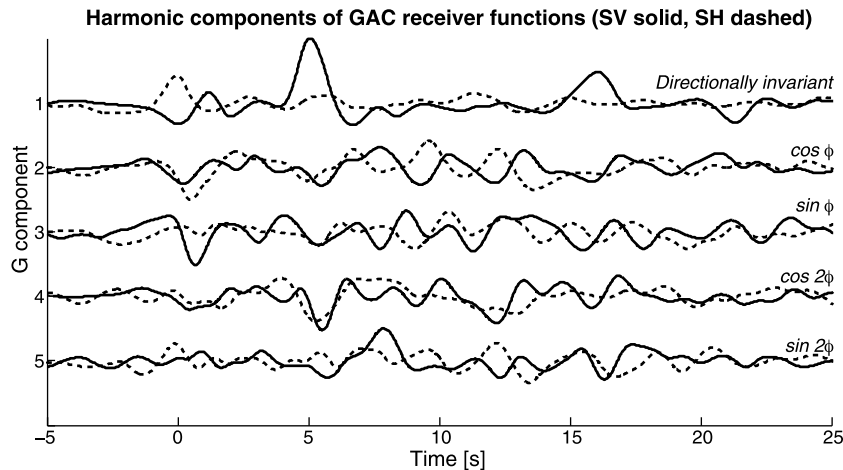


**Figure 9.** Harmonic receiver-function components recovered for station GAC, obtained by inverting for directionally invariant,  $\phi$ -periodic and  $2\phi$ -periodic backazimuthal components.

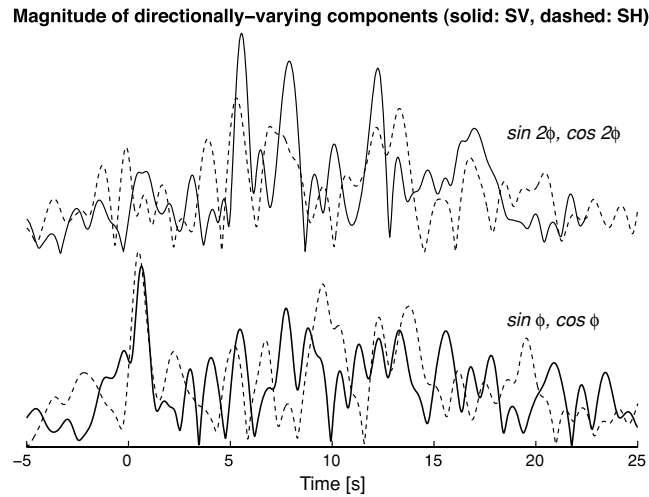


**Figure 10.** Magnitudes of the directionally varying harmonic components for station GAC. The  $2\phi$ -periodic components (upper) are commonly associated with horizontal-axis anisotropy, which the  $\phi$ -periodic components (below) are associated with dipping interfaces or plunging anisotropic axes.

amplitude at 0 s, implying an out-of-plane rotation of the  $P$  arrival, which could indicate a dipping interface in the near-surface. The peaks in the  $2\phi$ -periodic magnitude from 5–17 s suggest that arrivals with an anisotropic pattern occur at and below the Moho (the  $\approx 5$  s spike). This result is consistent with the model for GAC given in (Frederiksen *et al.* 2006), which consists of an isotropic crust underlain by multiple anisotropic layers. The extinction directions of the  $2\phi$  component will occur where  $2\phi = \arctan(-G_4/G_5)$ ; for the Moho peak, these directions average to  $\phi \approx 55^\circ, 145^\circ, \dots$ , which matches the sub-Moho fast direction obtained by Frederiksen *et al.* (2006) ( $155^\circ$ ).

It is worth noting that this formulation has an important deficiency with respect to a harmonic stacking approach: the absence of any moveout correction. By assuming that the receiver functions vary only with backazimuth, we have abandoned recovery of any variations with respect to  $q$  and so have given up our primary source of constraints on the seismic velocity. In addition, the failure to compensate for moveout limits the frequency band we can use, as the moveout causes a greater phase shift between traces at higher frequencies. One way around this would be to express  $G$  as the product of a harmonically varying backazimuthal pattern and a function of slowness, though we would then need to regularize the slowness function in some fashion.

## 7 ALTERNATIVE FORMULATIONS: MOVEOUT AND THE TIME DOMAIN

As implemented in Section 4 above, the panel deconvolution technique does not include any allowance for variation in arrival time and the intertrace constraints encourage traces to be identical regardless of their associated slowness. This has the benefit of making overregularization easier to recognize, as an excessive value for the  $\mu$  weighting factor will flatten arrivals across the deconvolved panel, eliminating moveout with respect to incidence angle. However, it also places an unrealistic condition on the receiver functions. The problem is more severe for the harmonic formulation given in section 6, as the harmonic formulation assumes that the receiver functions vary only with backazimuth.

Correcting for moveout is difficult to do in the frequency formulation given above. Corrections cannot be applied to traces prior to deconvolution, as the length of the source wavelet will cause arrivals with different moveout behaviour to overlap. The moveout cannot be accurately incorporated into the cross-trace constraints in the frequency domain, because the moveout operation is a non-linear stretching of the trace that cannot be reduced to a phase shift.

An alternative would be to pose the problem in the time domain. The convolution problem may be posed in the time domain in terms of the circulant matrix  $\mathbf{A}$  (*cf.* Ulyrch & Sacchi 2005), such that

$$s_j = \sum_{k=1}^N A_{jk} g_k = \sum_{k=1}^N p_{j-k+1} g_k. \quad (22)$$

With additional regularization constraints, this equation may be solved for  $\mathbf{g}$ . If damping is the only regularization used, the result will be essentially identical to damped frequency-domain deconvolution, though it will be much more computationally expensive due to the large size of the matrix. The advantage of a time domain formulation is that regularizations that are difficult to apply in the frequency domain (e.g. a regularization to favour sparse, spiky receiver functions) may be used.

One such regularization is cross-trace regularization with moveout constraints. Returning to our Delaunay triangulation, we can rewrite the cross-trace regularization on each triangle as

$$\frac{\partial g}{\partial q_N} \approx \frac{C_E - B_E}{n_z} g_A(t_A) + \frac{A_E - C_E}{n_z} g_B(t_B) + \frac{B_E - A_E}{n_z} g_C(t_C) = 0 \quad (23)$$

$$\frac{\partial g}{\partial q_E} \approx \frac{B_N - C_N}{n_z} g_A(t_A) + \frac{C_N - A_N}{n_z} g_B(t_B) + \frac{A_N - B_N}{n_z} g_C(t_C) = 0, \quad (24)$$

where the Green's function at each point of the triangle  $g_A$ ,  $g_B$ ,  $g_C$  may now correspond to a different time sample  $t_A$ ,  $t_B$ ,  $t_C$  determined using a moveout function; that is,  $t_A = t(\tau, q_A)$  where  $\tau$  is the zero-slowness time and  $q_A$  is the slowness corresponding to trace  $A$ . We can thus enforce similarity between time samples assumed to correspond to the same depth, rather than between samples corresponding to the same time. The only difficulty in implementation, compared to the frequency-domain case, is the large computational requirement; for the 114 traces and 2400 samples per trace of the GAC data set, cross-trace time domain deconvolution would require inverting a matrix of  $\approx 7 \times 10^{10}$  elements. However, for the much smaller problem of inverting only for harmonic backazimuthal components, a time domain approach appears feasible.

## 8 CONCLUSIONS

There is a middle ground between assuming that two traces arise from unrelated Green's functions, and assuming that their Green's functions are identical: penalizing the difference between the two. I have presented an implementation of this idea for panels of teleseismic receiver functions calculated at a single station. Intertrace constraints are imposed by minimizing the derivatives of the Green's function with respect to north-south and east-west slowness, the derivatives being posed in the Delaunay triangles formed by the location of each trace in  $(q_N, q_E)$  space. As shown using data from station GAC, the resulting 'panel deconvolution' both enhances the signal-to-noise ratio resolution and increases the recoverable frequency band. Panel deconvolution may prove to be of considerable assistance in recovering fine structure from receiver-function deployments, particularly at noisy sites. The idea of treating the Green's function as varying in space may be extended to harmonic analysis of receiver functions with respect to backazimuth, to recover patterns diagnostic of anisotropy or dipping structure.

## ACKNOWLEDGMENTS

Much of the work described here took place during sabbatical travel hosted by the Dublin Institute for Advanced Studies, Bristol University and the University of Leeds. The author is particularly grateful to his hosts at these institutions: Alan Jones, Sergei Lebedev, Michael Kendall and Sebastian Rost. Data from station GAC was obtained from the Canadian National Seismograph Network, operated by the Geological Survey of Canada. Travel was funded by the Dublin Institute of Advanced Studies; this research was supported by an NSERC grant. Helpful comments by two anonymous reviewers led to significant improvements in this paper.

## REFERENCES

- Agostinetti, N.P., Park, J. & Lucente, F.P., 2008. Mantle wedge anisotropy in Southern Tyrrhenian Subduction Zone (Italy), from receiver function analysis, *Tectonophysics*, **462**, 35–48.
- Ammon, C.J., 1991. The isolation of receiver effects from teleseismic  $P$  waveforms, *Bull. seism. Soc. Am.*, **81**, 2504–2510.
- Bendat, J.S. & Piersol, A.G., 1971. *Random Data: Analysis and Measurement Procedures*, 407 pp., Wiley-Interscience, New York.
- Bostock, M.B., 1998. Mantle stratigraphy and evolution of the Slave province, *J. geophys. Res.*, **103**, 21 183–21 200.
- Frederiksen, A.W. & Bostock, M.G., 2000. Modelling teleseismic waves in dipping anisotropic structures, *Geophys. J. Int.*, **141**, 401–412.
- Frederiksen, A.W. & Revenaugh, J., 2004. Lithospheric imaging via teleseismic scattering tomography, *J. geophys. Res.*, **109**, 978–990, doi:10.1111/j.1365-246X.2004.02414.x.
- Frederiksen, A.W., Ferguson, I.J., Eaton, D., Miong, S.-K. & Gowan, E., 2006. Mantle fabric at multiple scales across an Archean-Proterozoic boundary, eastern Ontario, Canada, *Phys. Earth planet. Inter.*, **158**, 240–263.
- Girardin, N. & Farra, V., 1998. Azimuthal anisotropy in the upper mantle from observations of P-to-S converted phases: application to southeast Australia, *J. geophys. Res.*, **103**, 615–629.
- Kind, R., Kosarev, G.L. & Petersen, N.V., 1995. Receiver functions at the stations of the German Regional Seismic Network (GRSN), *Geophys. J. Int.*, **121**, 191–202.
- Langston, C.A., 1979. Structure under Mount Rainier, Washington, inferred from teleseismic body waves, *J. geophys. Res.*, **84**, 4749–4762.
- Levin, V. & Park, J., 1998. P-SH conversions in layered media with hexagonally symmetric anisotropy: a cookbook, *Pure appl. Geophys.*, **151**, 669–697.
- North, R.G. & Basham, P.W., 1993. Modernization of the Canadian National Seismograph Network, *Seism. Res. Lett.*, **64**, 41.
- Okabe, A., Boots, B. & Sugihara, K., 1992. Spatial tessellations: concepts and applications of Voronoi Diagrams, in *Wiley Series in Probability and Statistics*, J., Wiley, Chichester, 532 pp.
- Savage, M.K., 1998. Lower crustal anisotropy or dipping boundaries? Effects on receiver functions and a case study in New Zealand, *J. geophys. Res.*, **103**, 15 069–15 087.
- Thompson, R.O.R.Y., 1979. Coherence significance levels, *J. Atmos. Sci.*, **36**, 2020–2021.
- Ulrych, T.J. & Sacchi, M.D., 2005. Information-based inversion and processing with applications, in *Handbook of Geophysical Exploration: Seismic Exploration*, Vol. 36, eds, Helbig, K. & Treitel, S., Elsevier, Amsterdam, 436 pp.
- Vinnik, L.P., 1977. Detection of waves converted from P to SV in the mantle, *Phys. Earth planet. Inter.*, **15**, 39–45.
- Zhu, L. & Kanamori, H., 2000. Moho depth variation in southern California from teleseismic receiver functions, *J. geophys. Res.*, **105**, 2969–2980.